

The 2020 M_w 6.4 Koryak Highlands earthquake illustrates hidden seismic hazards in the northern Pacific Cordillera

Guy Salomon¹, Edwin Nissen^{1,2}, Fengzhou Tan^{1,3}, Eric Bergman⁴,
Alastair Sloan⁵ and Léa Pousse-Beltran^{1,6}

¹*School of Earth and Ocean Science, University of Victoria, 3800 Finnerty Rd, Victoria, BC V8P 5C2, Canada. E-mail: guysalomon@uvic.ca*

²*College of Earth, Ocean, and Atmospheric Sciences, Oregon State University, 101 SW 26th St, Corvallis, OR 97331, USA*

³*Scripps Institution of Oceanography, University of California San Diego, 8622 Kennel Way, La Jolla, CA 92037, USA*

⁴*Global Seismological Services, Golden, CO 80401, USA*

⁵*Department of Geological Sciences, University of Cape Town, Rondebosch 7700, South Africa*

⁶*ISTerre, Université Grenoble Alpes, Université Savoie Mont Blanc, CNRS, IRD, Grenoble, 38058, France*

Accepted 2025 January 21. Received 2025 January 5; in original form 2024 October 30

SUMMARY

On 2020 January 9, an M_w 6.4 earthquake struck the central Koryak Highlands of eastern Siberia, northeast of the diffuse triple junction between the North American, Pacific and Eurasian plates. The largest earthquake recorded in the central Koryak Highlands to date, it provides an excellent opportunity to study the little-known active tectonics of this remote, sparsely instrumented region. We mapped coherent, coseismic surface deformation with Sentinel 1 Interferometric Synthetic Aperture Radar (InSAR), making this one of the highest latitude earthquakes to be captured successfully with satellite radar, in spite of the rugged, snow-covered terrain. Elastic dislocation modelling, teleseismic backprojections, calibrated hypocentral relocations and teleseismic moment tensor solutions are used to resolve a left-lateral fault trending northwestwards, proximal but perpendicular to a regional geological suture zone, the Khatyrka–Vyvenka Thrust. The earthquake probably ruptured unilaterally northwestwards along a 20 km long segment that appears indistinct in the local topography, and likely generated no surface rupture. We interpret that these observations are indicative of a structurally immature fault zone and estimate a seismogenic zone thickness of 10–15 km. The Koryak Highlands earthquake illustrates how terrane boundaries within cordilleran belts may continue to accommodate tectonic strain long after accretion, resulting in significant earthquakes even along hidden faults.

Key words: Radar interferometry; Seismic cycle; Asia; North America; Seismicity and tectonics.

1 INTRODUCTION

On 2020 January 9 at 08:38 UTC, a shallow, M_w 6.4 earthquake struck the Koryak Highlands of eastern Siberia, located in the westernmost North American cordillera and within a diffuse triple junction with the Eurasian and Pacific plates. The Koryak Highlands are an amalgamation of mountain ranges created through the Mesozoic–Palaeogene accretion of terranes onto the North American plate via northward subduction of the Pacific (Fig. 1). A series of NE-trending sutures and faults such as the Khatyrka–Vyvenka zone (Imaeva *et al.* 2017), bounded in the south by the Vatyna–Vyvenka thrust (Chekhovich *et al.* 2008), are relics of this process. Modern day regional seismicity is concentrated in the south-western Khatyrka–Vyvenka zone adjacent to the Kamchatka peninsula (Fig. 1), where notable events include the 2006 M_w 7.6 and 6.6 Olyutorskii and 1991 M_w 6.6 Khailino reverse faulting earthquakes (Lander *et al.* 1996,

2010; Rogozhin *et al.* 2007). Seismicity decays northeastwards towards the central Koryak Highlands, where the largest events prior to 2020 were M_w 5.6 and 5.3 strike-slip earthquakes in 1988 and 2007 (Lander *et al.* 1996; Rogozhin *et al.* 2021). The larger, M_w 6.4 2020 earthquake thus offers an opportunity to better understand the little known active tectonics of this region, and whether inherited geological structures influence modern seismicity.

This latter question is of much broader relevance. The geological formation of the Koryak Highlands is characteristic of the northern Pacific Cordillera, defined here as the part of the circum-Pacific orogenic system where Pacific oceanic lithosphere subducts below the continental North American plate, and stretching from Kamchatka in the west to Haida Gwaii in the east (Fig. 1, inset). Allochthonous terranes accreted onto the western margin of the North American continent throughout the Mesozoic and early Cenozoic eras (Coney & Evenchick 1994; Dickinson 2004; Akinin *et al.* 2020),

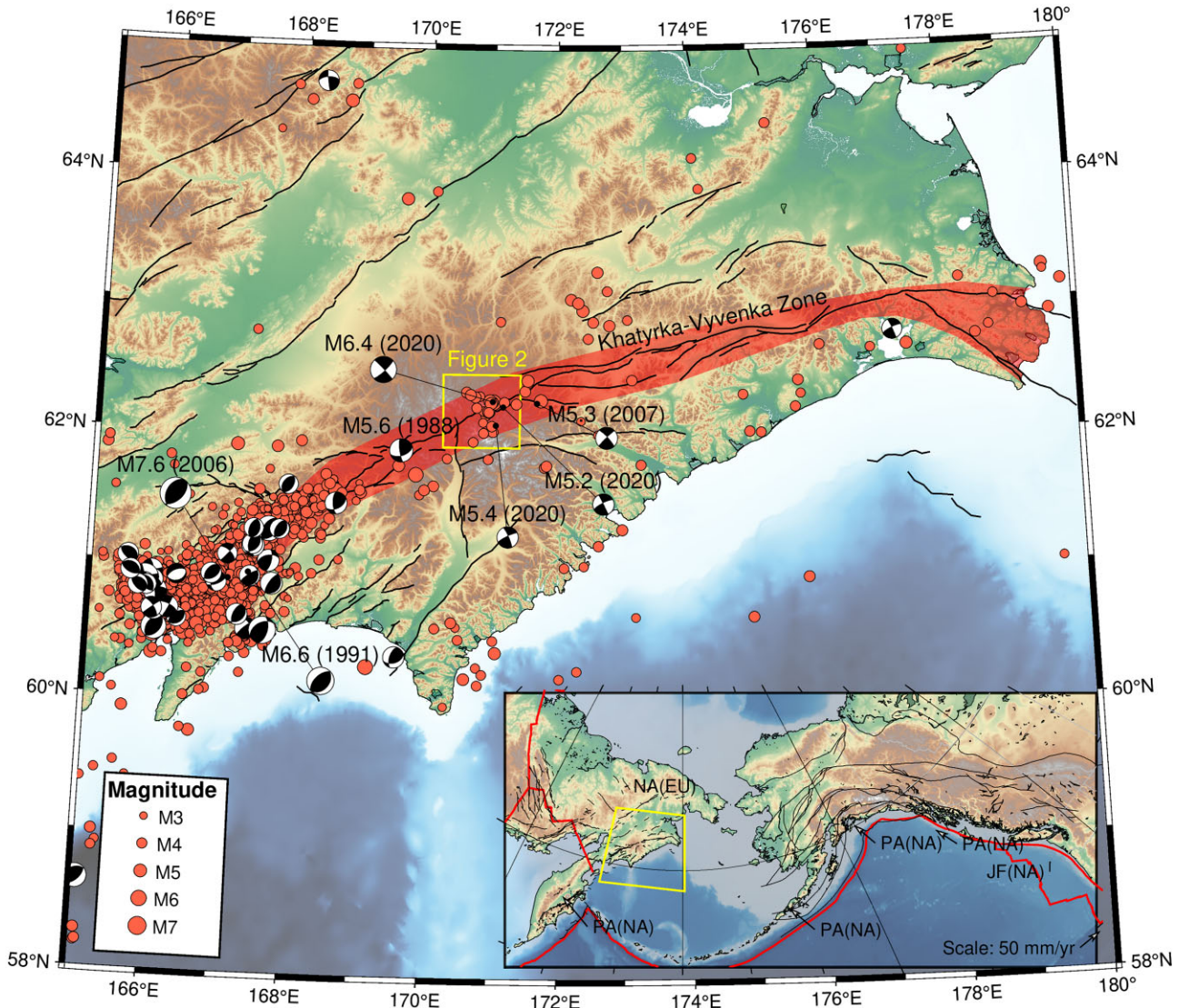


Figure 1. Seismicity and active faulting within the Koryak Highlands. Red dots are $M 2.5+$ epicentres for 1960–2024 from the International Seismological Centre (2024) and focal mechanisms are from the GCMT catalogue (Dziewonski *et al.* 1981; Ekström *et al.* 2012); note the change from predominantly thrust faulting in the SW (near the Kamchatka Peninsula) to strike-slip mechanisms within the central Koryak Highlands. Faults are from Zelenin *et al.* (2022) with the Khatyrka–Vyvenka Zone marked by a red transparent polygon. Background topography is the Copernicus GLO90 DEM (European Space Agency, Singergise 2021) and bathymetry is from the GEBCO Compilation Group (2023). Inset shows the location of the main map (yellow polygon) within the broader North Pacific Cordillera, with major structures in Alaska and Canada from the Yukon Geological Survey (2011). Vectors show relative velocities of the Pacific (PA), North American (NA), Eurasia (EU) and Juan de Fuca (JF) plates from the ITRF2020 plate motion model (Altamimi *et al.* 2023).

with deformation apparently slowing into the late Cenozoic, but not stopping altogether. Understanding the causes and characteristics of crustal seismicity within the Koryak Highlands, and in particular its links to inherited geological structure, may therefore inform our understanding of the potential for large earthquakes in other parts of the northern Pacific Cordillera (e.g. Wetmiller *et al.* 1988; Gaudreau *et al.* 2019). Though very few people live in the Koryak Highlands, large earthquakes may pose risks to vulnerable population centres and critical infrastructure in these neighbouring regions.

The central object of this study is to characterize the 2020 earthquake sequence in as much detail as possible, notwithstanding its remote location which poses a number of methodological challenges. We build on a preliminary seismological analysis of the sequence by Rogozhin *et al.* (2021) and an Interferometric Synthetic Aperture

Radar (InSAR) study of the main shock by Sviggas *et al.* (2023), which notably disagree on which of the seismological nodal planes the earthquake ruptured. We resolve this by performing our own analysis and modelling of InSAR data, revealing the main shock geometry and slip distribution and in doing so helping to constrain the regional seismogenic layer thickness. However, we also add a number of new seismological constraints, relying upon teleseismic data in the absence of local and regional station coverage. We use body waveform analysis to constrain and independently check the main shock geometry and centroid depth, a phase-weighted back-projection to reveal the main shock kinematics, and a calibrated earthquake relocation in order to assess the aftershock distribution which has the potential to delineate other, neighbouring active structures. We finish by discussing implications for active tectonics and earthquake hazards within the northern Pacific Cordillera.

2 METHODS

2.1 InSAR

The 2020 Koryak Highlands earthquake was captured by the European Space Agency's (ESA) Sentinel 1A satellite on descending track 118D and ascending tracks 125A and 154A. All of the available 12 or 24 day coseismic interferograms, including some post-seismic pairs, were processed using GAMMA software (Werner *et al.* 2000), topographic effects were removed using the 30 m-resolution Copernicus digital elevation model (DEM, GLO-30), and the interferometric phase was unwrapped using the minimum cost flow algorithm (Werner *et al.* 2002) before being converted from radar to geographic coordinates (WGS-84) and from radians to line-of-sight (LOS) displacement. Large parts of many of the interferograms have poor coherency owing to the high latitude, rugged topography, and wintertime acquisitions, all of which can cause decorrelation (Wang *et al.* 2020). The shorter repeat acquisition times of Sentinel 1 over earlier generations of SAR satellites offer an vast improvement for wintertime imaging at high latitudes (e.g. Elliott *et al.* 2007; Mikhailov *et al.* 2023). A clear coseismic signal is evident on a 12 day interferogram (2020 January 03–15) on descending track 118D and on a 24 day interferogram (2019 December 23–2020 January 16) on ascending track 125A. A 12 day interferogram on the adjacent track 154A also exhibited coseismic deformation but was too noisy to be useful in the modelling stage and is not discussed further.

To characterize the causative faulting, the LOS displacements were first downsampled using a quadtree algorithm (Jónsson *et al.* 2002) and then inverted for uniform slip on a rectangular dislocation embedded within an elastic half-space with Lamé parameters $\mu = \lambda = 3.2 \times 10^{10}$ Pa (Okada 1985). Weighting the two data sets equally, we solved for the fault strike, dip, rake, slip, surface projection centre points, length and top and bottom depths, using a nonlinear, downhill Powell's algorithm (Press *et al.* 2007) with 100 Monte Carlo restarts to avoid local minima (Wright *et al.* 1999). To account for satellite orbital errors and different unwrapping reference points, we also jointly solved for linear ramps and static shifts in LOS displacement. To achieve the best possible fit to the observed data in a stable inversion, we found it preferable to fix the slip to 0.9 m to ensure that the modelled deformation had the same number of fringes as the observed interferogram. This value was chosen on the basis of fault scaling relationships (Kanamori & Anderson 1975).

To resolve finer details, we solved for the distribution of slip across the model fault plane. The fault plane was first extended along strike and downdip, and then subdivided into $1 \text{ km} \times 1 \text{ km}$ patches. The slip on each patch was estimated using a Laplacian smoothing operator (Wright *et al.* 2004; Funning *et al.* 2005) and a non-negative least-squares algorithm to ensure positive slip (Bro & De Jong 1997). A range of smoothing factors were tested so as to obtain a realistic, non-oscillatory slip gradient without unduly increasing the misfit.

2.2 Seismic body wave analysis

We used long-period teleseismic body-waveform modelling as an independent check of the main shock focal mechanism and centroid depth. Waveform data were restricted to epicentral ranges of 30° – 90° for P waves and 30° – 80° for SH waves in order to avoid complications from unmodelled lithosphere and core phases. 26 vertical component P -wave seismograms and 24 transverse component

SH -wave seismograms were selected for modelling on the basis of high signal-to-noise ratios and an even global distribution without any large azimuthal gaps. We used the MT5 program (Zwick *et al.* 1994) developed from the algorithms of McCaffrey & Abers (1988) and McCaffrey *et al.* (1991) to minimize differences between the observed waveforms and synthetic seismograms calculated using a half-space with $V_p = 6.0 \text{ km s}^{-1}$, $V_s = 3.5 \text{ km s}^{-1}$ and density = 2800 kg m^{-3} (values consistent with the elastic parameters used in our InSAR modelling). The synthetic seismograms incorporate direct P and SH phases and pP , sP and sS depth phases, thus providing sensitivity to centroid depth (Molnar & Lyon-Caen 1989; Wimpenny & Watson 2021), and represent the source time function as the combination of a series of triangular elements, with the moment being their integral. Before inversion, the synthetic P and SH waveforms were aligned against their observed arrivals on broad-band vertical and transverse seismograms so as to remove any potential influence from epicentral mislocation. The program uses a least-squares routine to solve for the centroid strike, dip, rake, depth and source time function by minimizing misfits between observed and synthetic seismograms. To test the sensitivity of the solution to varying centroid depth, we then fixed this parameter in 1 km increments either side of the minimum misfit value and re-ran the inversion allowing the strike, dip, rake and source time function to vary (Molnar & Lyon-Caen 1989; Nissen *et al.* 2014).

2.3 Backprojection

We assessed the rupture kinematics using the phase-weighted relative backprojection method (Schimmel & Paulssen 1997; Zhang & Ge 2010; Tan *et al.* 2019). Relative energy (RE) was backprojected onto a 0.01° ($\approx 1 \text{ km}$) grid across the source region using a teleseismic array in the contiguous United States and traveltimes estimated with the IASP91 reference model (Kennett & Engdahl 1991). We also tested a European array, but the results showed considerable swimming artefacts (Meng *et al.* 2012), likely reflecting that while source–receiver paths to the US are approximately perpendicular to the NW-trending fault, those to Europe lie roughly along strike. An additional issue could be the epicentral distance to the EU array being significantly larger (62° – 77°) than to the US array (40° – 65°), as such, the signal-to-noise ratio for the EU array is lower than for the US array. The P seismograms were aligned using cross-correlation, the waveforms were then stacked using a 10 s sliding window. A frequency band of 0.2–2 Hz was used, the waveform amplitudes were normalized, and the RE was calculated using phase-weighted stacking to reduce biases introduced by incoherent signals with large amplitudes. The sliding window produced some artefacts in the form of energy radiators centred upon the same source grid node but at different times; here, the mean source times were chosen and the rest were discarded.

2.4 Calibrated relocation

The hypocentral locations of the 2020 main shock, an M_1 4.1 foreshock, 15 aftershocks (m_b 3.6– M_1 5.4), and 22 other events located within a radius of 1.5° were re-evaluated using the *mloc* calibrated earthquake relocation software (Bergman & Solomon 1990; Walker *et al.* 2011). We acquired phase data from the ISC bulletin (International Seismological Centre 2024) and only included events with 30 or more phase readings in the relocation. The *mloc* program minimizes location bias by exploiting the fact that ray paths of events clustered in space and recorded at common stations sample roughly

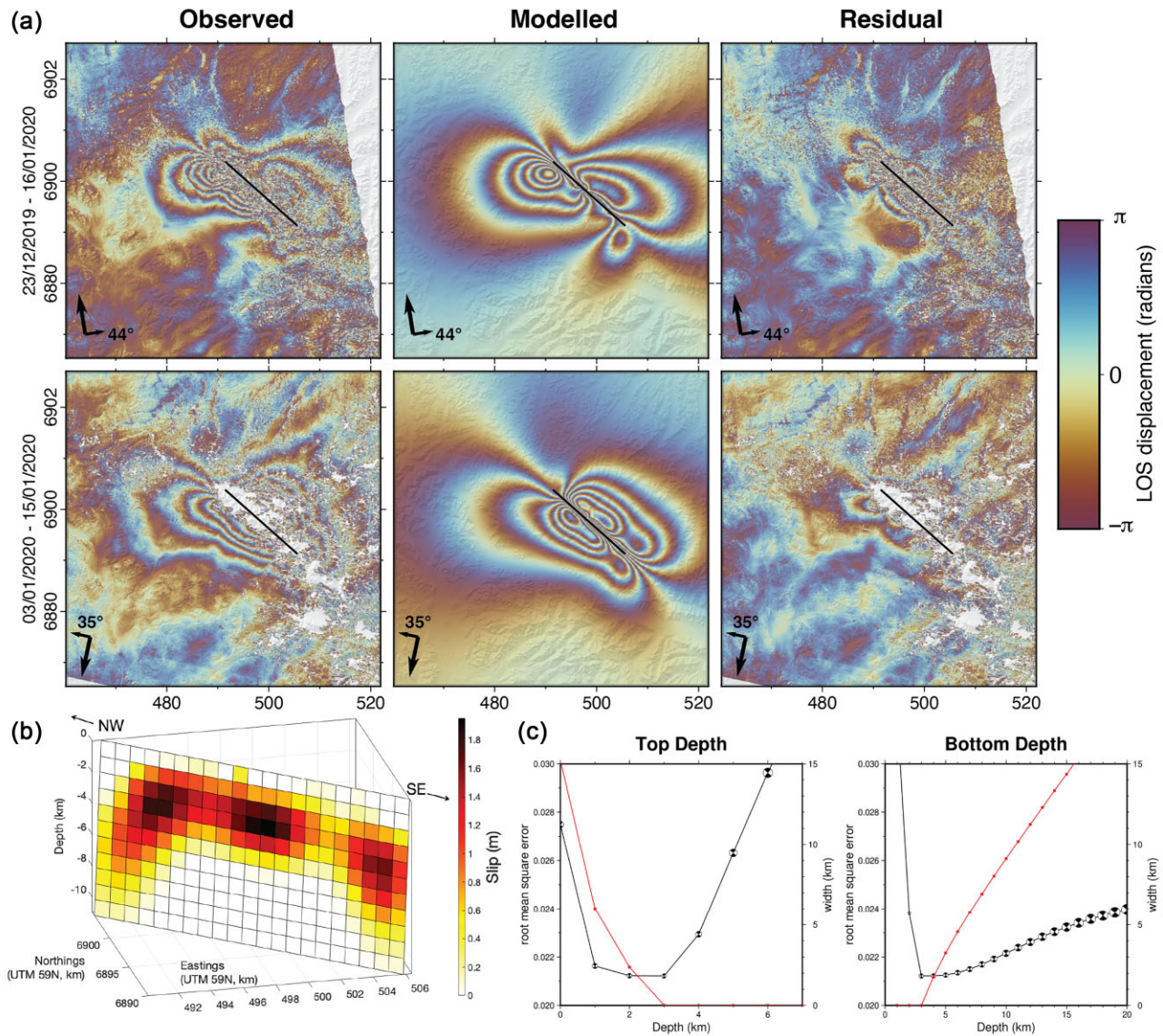


Figure 2. (a) Top row: (left) observed 24 day, (middle) model and (right) residual interferograms for Sentinel 1 ascending track 125. Bottom row: (left) observed 12 day, (middle) model and (right) residual interferograms for descending track 118. To better visualize the shape of the displacement field, all interferograms are left wrapped, with 2π radians equivalent to 2.77 cm LOS displacement. Large and small arrows show satellite track and LOS azimuths, along with the incidence angle measured from the vertical at the earthquake. The black line is the surface trace of our InSAR model fault. Coordinates are in UTM kilometres (Zone 59N). (b) Modelled slip distribution on 1 km \times 1 km fault patches. (c) Uniform slip parameter sensitivity tests for (left) model fault top depth and (right) bottom depth, with root mean square error (black line) calculated at fixed 1 km increments and the inversion re-run with all other parameters free to vary. Focal mechanisms show how strike, dip, rake and magnitude parameters varied for each run. The red line is the implied rupture width for each inversion.

the same portion of the Earth, such that traveltime differences more likely represent the relative epicentre locations within the cluster rather than the 3D velocity structure. The relocation is split into two independent steps, each using a specific, tailored set of arrival time data (Jordan & Sverdrup 1981). The first step estimates the relative locations of each hypocentre within the cluster using differences in arrival times at common stations at all distances. For the second step, we used an indirect calibration to constrain the absolute location of the hypocentroid. Indirect calibration makes use of a precise, independent constraint on the epicentre of at least one earthquake in the sequence (Walker *et al.* 2011); we chose to place the main shock epicentre along the trace of our InSAR model fault where it roughly bisects the cloud of well-located aftershocks.

Without any close-in stations or even much in the way of regional coverage, we are heavily reliant on teleseismic depth phases to solve for focal depths. Unfortunately, we find that those reported for earthquakes in our relocation cluster are often unreliable, with some stations offering only theoretical depth phase arrival times based on a preliminary hypocentre, and others listing identical pP and sP arrival times. Because of this, we were unable to solve for the best-fitting focal depths for most of the earthquakes within the 2020 cluster. We were able to constrain a focal depth for the main shock, but for all other events the focal depth was set to 10 km, consistent with independent inferences of the main shock centroid depth and seismogenic layer thickness, described below. Based on prior experience, we do not anticipate there to be any meaningful

Table 1. Source parameters of the 2020 January 9 Koryak Highlands main shock, from the GCMT, USGS ANSS Comprehensive Earthquake Catalog, GEOFON, Svigkas *et al.* (2023) InSAR model, and from our own modelling. Location refers to the GCMT and GEOFON centroids, the USGS epicentre and the peak slip patch our InSAR model (surface projection coordinates of our InSAR model fault planes are listed separately in Supporting Information, Table S1). Depth refers to the centroid depth for all of the seismological solutions, and the depth of peak slip for the InSAR solutions. The asterisks caution that automated centroid depths of the GCMT, USGS and GEOFON catalogues are unreliable for shallow continental earthquakes and are often assigned fixed values (e.g. Wimpenny & Watson 2021).

Source	Location	Strike	Dip	Rake	Depth	Moment (Nm)	M_w
GCMT	62.27°, 171.00°	316°	86°	−11°	12 km*	4.38×10^{18}	6.4
USGS W-phase	62.358°, 171.061°	317°	88°	−13°	19.5 km*	4.60×10^{18}	6.4
USGS body wave	62.358°, 171.061°	320°	85°	−3°	13 km*	3.09×10^{18}	6.3
GEOFON	62.33°, 170.94°	135°	85°	0°	10 km*	3.60×10^{18}	6.3
Svigkas <i>et al.</i> (2023)	62.214°, 170.931°	304°	86°	−3.2°	2.5 km	3.87×10^{18}	6.3
This study (InSAR)	62.203°, 170.986°	132°	86°	4°	3.5 km	3.71×10^{18}	6.3
This study (body waves)	—	317°	85°	0°	9 km	3.22×10^{18}	6.3

impact on epicentral accuracy from this choice of fixed focal depth (e.g. Ghods *et al.* 2012; Karasözen *et al.* 2016).

3 RESULTS

3.1 Main shock

The InSAR data and modelling provide the best constraints on the main shock location and geometry. The interferograms are generally coherent, though steep topography and/or snow cover (Fig. S1, Supporting Information) may have introduced noise to the mountainous, eastern parts (Fig. 2a, left panels). Both interferograms also contain an NW-trending band of partial decorrelation, clearest in the descending scene in which it is masked out in Fig. 2(a) (lower left panel). Nevertheless, coseismic deformation appears clearly in both interferograms as two main fringe lobes, one on each side of the decorrelation band. The western lobes contain the peak displacements, which are toward the descending track satellite and away from the ascending satellite, while the eastern lobes show the opposing sense of motion. This pattern is consistent with left-lateral motion along a fault aligned northwest–southeast, roughly along the observed band of decorrelation. The ascending interferogram also exhibits smaller deformation lobes at either end of the faulting, which is as expected since its look vector is more oblique to fault strike than the descending one.

Inversion of downsampled InSAR data for uniform slip on a rectangular model fault can reproduce the observed deformation well, with root-mean-square residual LOS displacements of 2.17 cm (Figs S2 and S3, Supporting Information). The best-fitting fault is 19.2 km long, trends NW–SE along the decorrelation zone (strike 132°), dips steeply SW (86°), and has left-lateral slip (rake 4°). Given elastic rigidity of 3.2×10^{10} Pa, this gives rise to a moment of 3.88×10^{18} N·m (equivalent to M_w 6.3), in the middle of the range of available seismological estimates (3.1 – 4.6×10^{18} N·m, Table 1). Our results are in reasonable agreement with those of Svigkas *et al.* (2023), with discrepancies of <15 per cent in uniform slip, fault length, and width, and of 8° in strike, <1° in dip (which they fixed), and 7° in rake. However, our InSAR model fault geometry has closer consistency than Svigkas *et al.*'s with the NW-striking seismological nodal planes, with discrepancies in strike, dip and rake ranging from just 2°–4° for the GEOFON model to 4°–15° for those of the United States Geological Survey (USGS) and Global Centroid Moment Tensor (GCMT) catalogues (Table 1). To explore the possibility of along-strike rupture segmentation, we also tried inversions with two rectangular uniform slip fault planes (Elliott *et al.* 2012), but found that these did not visually improve the fit to the

data despite double the number of free parameters (Figs S5 and S6, Supporting Information). This result is consistent with the unusually high percentage (96–98 per cent) double couple components of the reported USGS moment tensors, which imply a simple, planar earthquake source (e.g. Zaccagnino & Doglioni 2022).

We tested the sensitivity of our uniform slip model to fault top and bottom depths by incrementally altering these parameters and assessing the effects on model misfit. When the top depth is reduced to zero, the misfit rises markedly, suggesting that the rupture did not reach the surface (Fig. 2c). When the top depth is increased to 2–3 km, the misfit remains low but the fault width becomes unreasonably narrow. The bottom depth is less well constrained, with the misfit rising only gradually as the bottom depth is lowered from ~5 km.

Our distributed slip InSAR inversion provides a more refined indication of the depth limits of coseismic slip as well as its variation along strike. In our preferred model, root-mean-square residual displacements are reduced by about a quarter from those of the uniform slip model to 1.66 cm, and the visual fit to the data is also improved (Fig. 2a and Fig. S3, Supporting Information), with removal of some residual fringes present in the uniform slip model interferograms (Figs S1 and S2, Supporting Information). Model slip peaks at 1.9 m at a depth of ~3.5 km along the middle portion of the fault, with two distinct slip asperities near the NW and SE fault ends (Fig. 2b). Only a small proportion of the slip reaches the shallowest row of model fault patches, supporting our earlier inference of a substantial shallow slip deficit (SSD). At the base of the model slip patch, slip tails off abruptly at 5–6 km depth beneath the central slip asperity and more gradually at 7–10 km beneath the distal ones. The InSAR moment of 3.71×10^{18} N·m (equal to M_w 6.3) is in agreement with the equivalent seismological values of 3.1 – 4.6×10^{18} N·m (Table 1). Our slip model with its three asperities and pronounced SSD qualitatively resembles the pattern resolved by Svigkas *et al.* (2023), though a direct comparison is impossible since their model is not tabulated.

Our body waveform modelling can reproduce observed teleseismic P and SH waveforms well with purely double couple motion lasting 12 s (Fig. 3a), further confirmation of a simple, planar fault source. The best solution has an NW-trending nodal plane with strike 317°, dip 85° NE and rake 0° (Table 1). This geometry is closely consistent with our InSAR model fault plane, with differences of just 4°–9° in strike, dip and rake, accounting for the opposing dip direction and application of the right-hand rule. The minimum misfit centroid depth of 9 km is somewhat deeper than our InSAR model fault centre and peak slip depths of ~4–5 km. However, centroid depth sensitivity tests (Fig. 3b) reveal similarly low misfits for

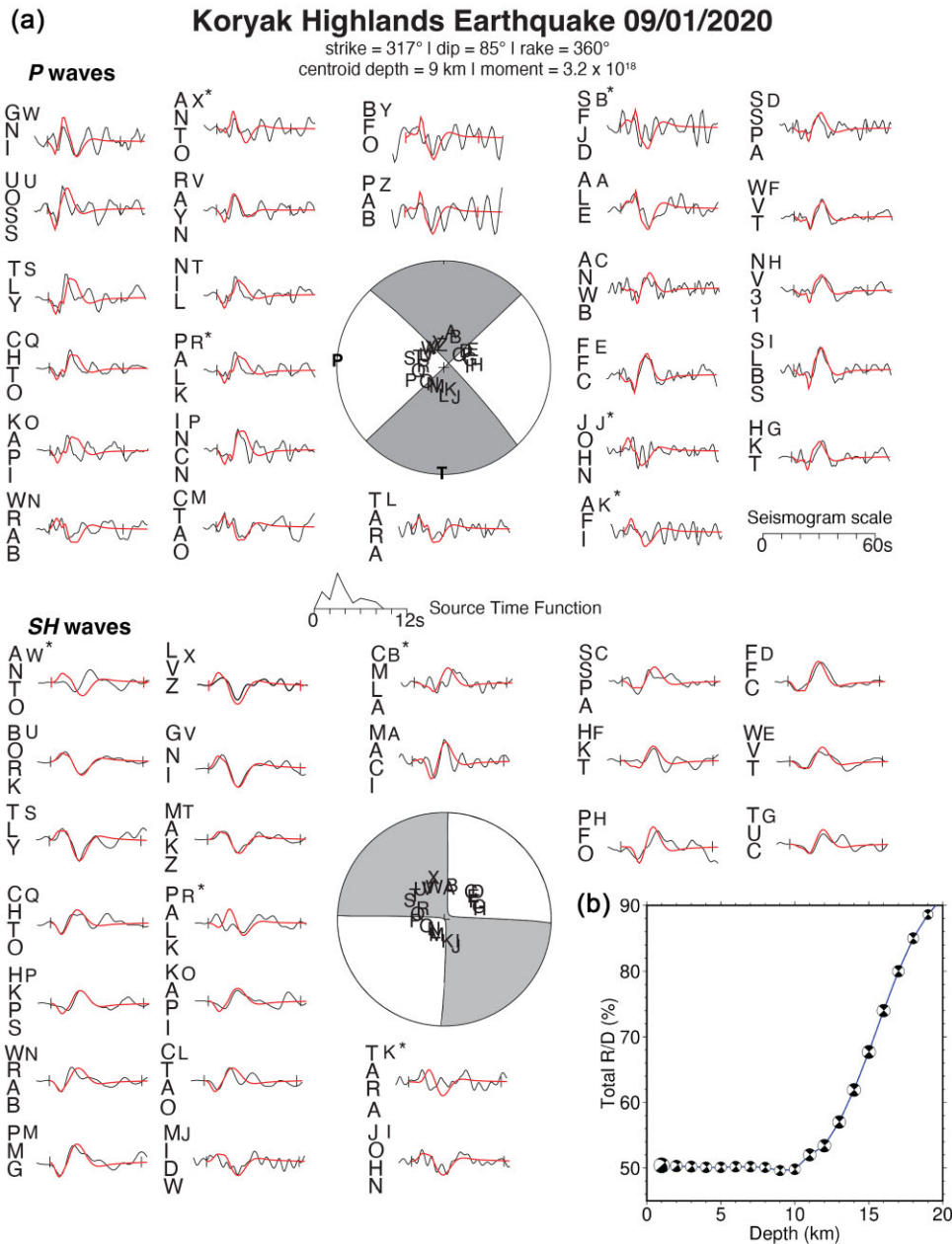


Figure 3. (a) Teleseismic body waveform model of the 2020 January 9 earthquake. The stereoplots show the (top) *P* and (bottom) *SH* focal spheres, with stations marked by capital letters and *P*- and *T*-axes in bold. Surrounding each focal sphere are the observed (black) and synthetic (red) vertical (*P*) and transverse component (*SH*) seismograms, with station codes written vertically beside the stereoplot characters, and vertical ticks marking the inversion window with the time scale shown middle right. The source time function is in the centre of the figure. (b) Results of our centroid depth uncertainty tests, with the per cent of weighted residual variance (*R/D*) plotted along with model strike, dip and rake at 1 km increments of fixed depth.

depths ranging from 3–10 km with relatively small consequences to model strike, dip, rake and magnitude. Only below 10 km do body-waveform model misfits increase markedly, while above 3 km, the misfit remains low but the NW-striking nodal plane inclines to an anomalously shallow angle. This result is within agreement with the focal depth of 13 km calculated during relocation in *mloc*, assuming that slip propagated upwards after nucleating near the base of the rupture plane (e.g. Karasözen *et al.* 2016; Wei *et al.* 2015).

To investigate discrepancies in fault plane geometry between the various available main shock focal mechanisms (Table 1), which are important for understanding regional kinematics, we tested the sensitivities to strike and dip direction of our InSAR and teleseismic

body waveform models. We repeated our InSAR uniform slip and body waveform inversions with strike values kept fixed at small (2° – 5°) increments either side of the minimum misfit values, and recorded the root-mean-square error or normalized error for each model run (Fig. 4). When the waveform model is assigned our preferred InSAR model strike of 132° (Fig. 4, red line), the resulting normalized error is only marginally greater than the minimum misfit value, whereas when the InSAR model is assigned our preferred waveform model strike of 317° (green line), the resulting root-mean-square error is conspicuously larger than the minimum misfit value. This leads us to favour the strike and south-westward dip direction yielded by our InSAR modelling. The broader minima in

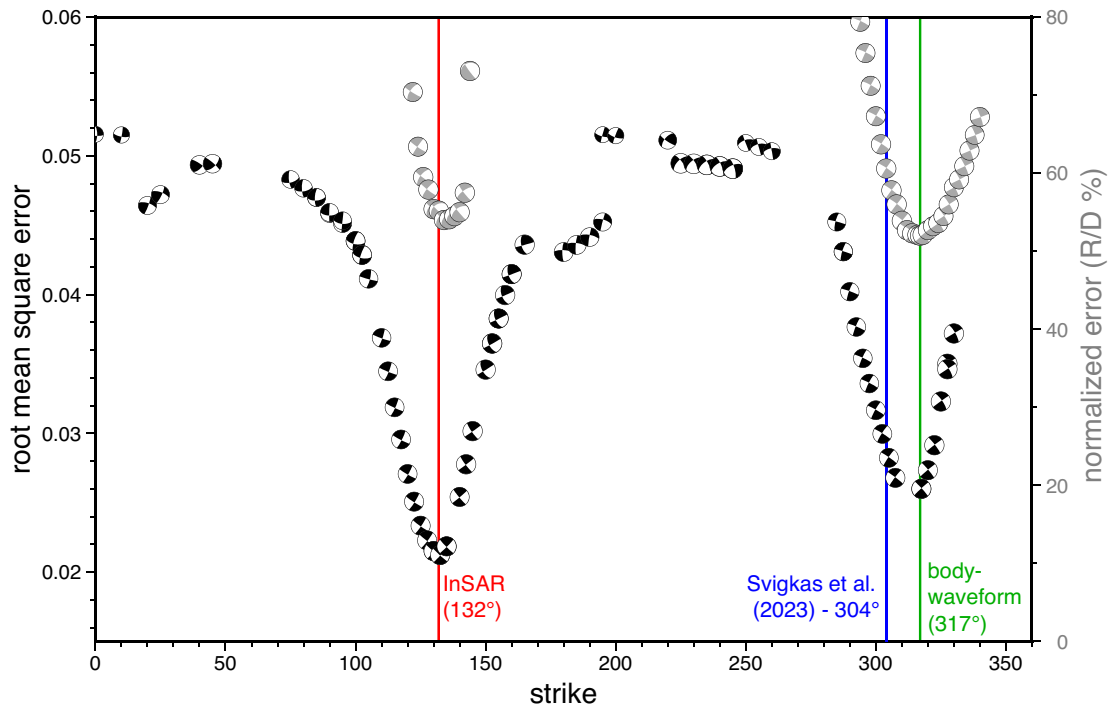


Figure 4. Strike sensitivity tests for InSAR and teleseismic body-waveform modelling of the 2020 January 9 Koryak Highlands main shock. InSAR (black) and waveform (grey) focal mechanisms are plotted as a function of their fixed strike values and root-mean-square error or normalized error (defined as the percentage ratio of the weighted residual variance to the weighted data variance, or R/D per cent). Red, blue and green lines shows strike values of our own InSAR model, the InSAR model of Sviggas *et al.* (2023) and our body waveform model, respectively.

the waveform modelling misfit curve may reflect the large azimuthal gap to the SE (Fig. 3), though uncertainties in the order of ± 5 – 15° are common for this procedure (Molnar & Lyon-Caen 1989). Notably, the strike of the InSAR model of Sviggas *et al.* (2023), which at 304° is 12° – 16° different from any of the other available solutions, falls outside of the minima in either of our misfit curves (Fig. 4, green line).

Our backprojection provides an independent check on the fault orientation and our best indication of the rupture kinematics, though we acknowledge that the earthquake is close to the M_w limit of 6.5 that this method can reliably resolve (Kiser & Ishii 2017). Our results indicate that slip propagated unilaterally northwestwards at an average rupture velocity of $\sim 1.3 \text{ km s}^{-1}$ (Figs 5a and d). Coherent backprojected energy is released over a duration of $\sim 14 \text{ s}$ (Fig. 5b), consistent with the 12 s source time function duration estimated from body waveform modelling (Fig. 3), and over a distance of $\sim 15 \text{ km}$ (Fig. 5c), similar to the 22 km length of our InSAR model fault, with peak energy release at $\sim 6 \text{ s}$ close to the epicentre.

3.2 Aftershock distribution

The original ISC epicentres for the 2020 sequence are highly scattered, but generally are located upon a step-over along the SW-trending Khatyrka–Vyvenka fault (Fig. 6a). Relocation shifts and condenses the events southwards to between the mapped traces of the Khatyrka–Vyvenka and Vatyn–Vyvenka faults, but the aftershock cloud still lacks any obvious structure or preferred orientation (Fig. 6b). Presumably, many of these aftershocks are rupturing unidentified faults secondary to both the main shock and the main suture zones. Notably, there is no concentration of events in the

inferred northwestward direction of main shock rupture propagation; in fact, the aftershock distribution is perhaps more favorably explained by a bilateral rupture. Additional maps, traveltime curves and residual plots associated with the relocation can be found in Figs S7–S11 (Supporting Information).

4 DISCUSSION

4.1 Fault geomorphology, structural immaturity and shallow slip deficit

Having located the main shock fault with InSAR, we investigate whether its surface trace corresponds with any fault-related geomorphology such as scarps, shutter ridges or stream offsets. We used a section of the 2 m resolution ArcticDEM DEM (Porter *et al.* 2022), downloaded with a buffer of several kilometres along the InSAR fault bounds (Fig. 7). This was hillshaded from several different directions, in order to highlight potential tectonic features no matter their orientation or facing directions. We observed rugged topography, with the fault trace crossing several drainage systems and ridgelines, including several cirques and one large valley, mostly at high angles. After inspection, there are no clear, fault-related lineaments or landforms in this area, so it is likely that the 2020 M_w 6.4 earthquake ruptured a structurally immature and/or slow slip-rate fault that has accumulated insufficient surface slip to imprint the postglacial landscape. The Koryak Highlands were glaciated at least twice during the Pleistocene, although these were mostly valley glaciers with little evidence for large ice sheets and domes (Glushkova 2011). This is consistent with the fault strike being orthogonal to the mature, terrane-bounding Khatyrka–Vyvenka

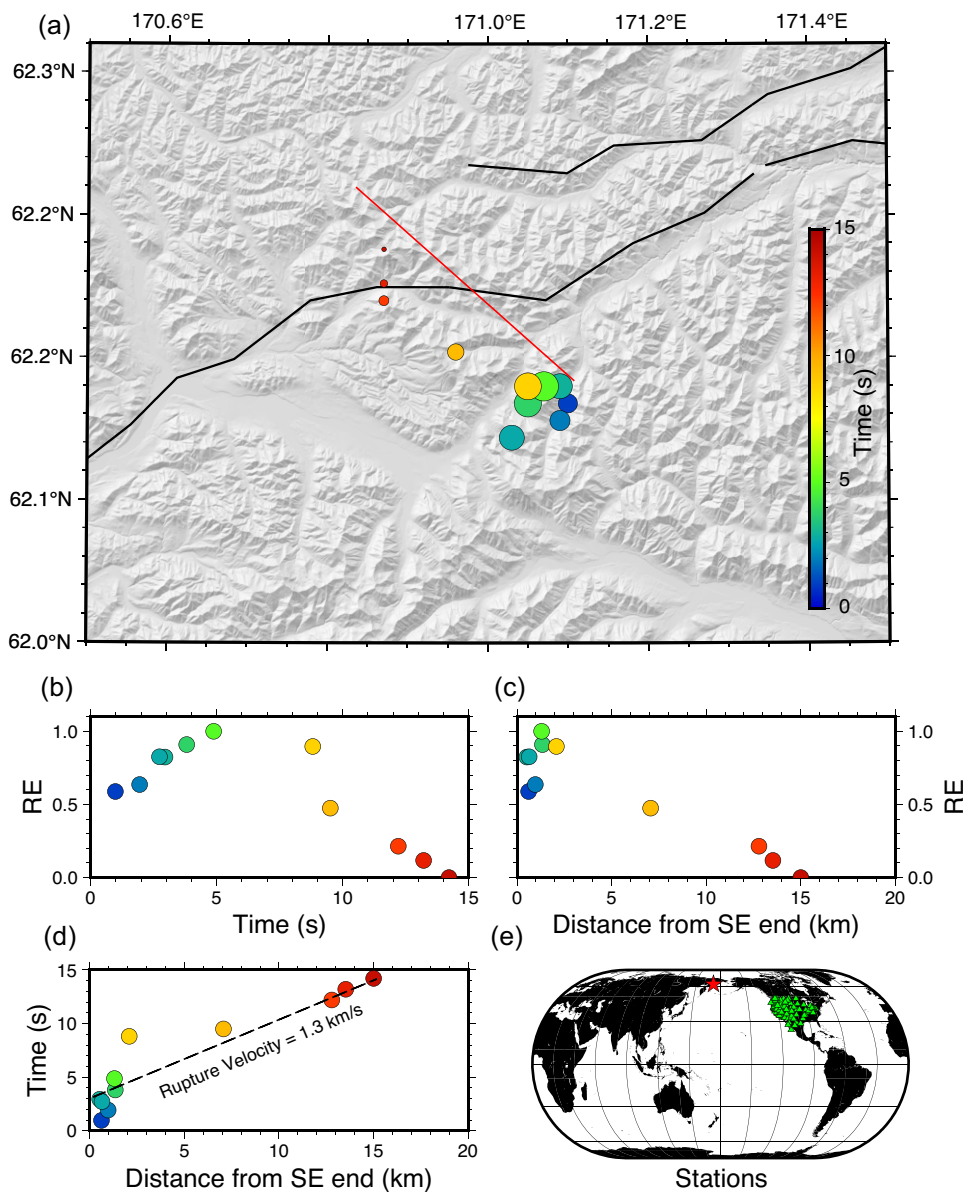


Figure 5. (a) Results of a phase-weighted backprojection using a contiguous US-based array. Colour scale shows the time since onset of the event while size shows the RE. Red line marks the InSAR modelled fault, black lines are mapped faults (Zelenin *et al.* 2022). (b) RE release versus time, where the RE has been normalized to 1. (c) RE and projected distance along the InSAR modelled fault. (d) Time versus the projected distance along the InSAR fault. (e) Stations (green triangles) used in the backprojection.

fault (Zelenin *et al.* 2022), which by contrast is relatively well expressed in the regional topography.

Other aspects of the 2020 earthquake sequence are also consistent with immature faulting. The propagation of the main shock rupture front imaged by backprojection is just $\sim 1.3 \text{ km s}^{-1}$, consistent with the slow rupture velocities expected along immature faults with many remaining asperities along the fault plane (Perrin *et al.* 2016; Guo *et al.* 2023). The scattered, off-fault aftershocks are another indication of structural immaturity, with seismic sequences along mature faults expected to cluster more narrowly along the principle shear zone (Perrin *et al.* 2021).

A final characteristic of the 2020 earthquake that may relate to fault structural immaturity is its pronounced SSD, the reduction in slip towards the Earth surface commonly observed in geodetic slip

models (e.g. Simons *et al.* 2002; Fialko *et al.* 2005). Understanding the causes of SSDs is important for seismic hazard assessment, and off-fault deformation in earthquakes on immature faults is one proposed mechanism (Dolan & Haravitch 2014). By constructing a normalized slip profile from our distributed slip InSAR model (Fig. 2b), we observe peak slip at 3–4 km depth diminishing by over 90 per cent at the surface (Fig. 8a, thick black line). Superimposing this onto a compilation of normalized slip profiles from 29 large strike-slip earthquakes with published InSAR slip models (Sethanant *et al.* 2023) highlights how a large subset of these earthquakes have similarly pronounced SSDs (Fig. 8a). Following Sethanant *et al.* (2023), we further classify these earthquakes by the total offset of the host fault – a measure of structural maturity – and by magnitude (Figs 8b and c). This shows how those with

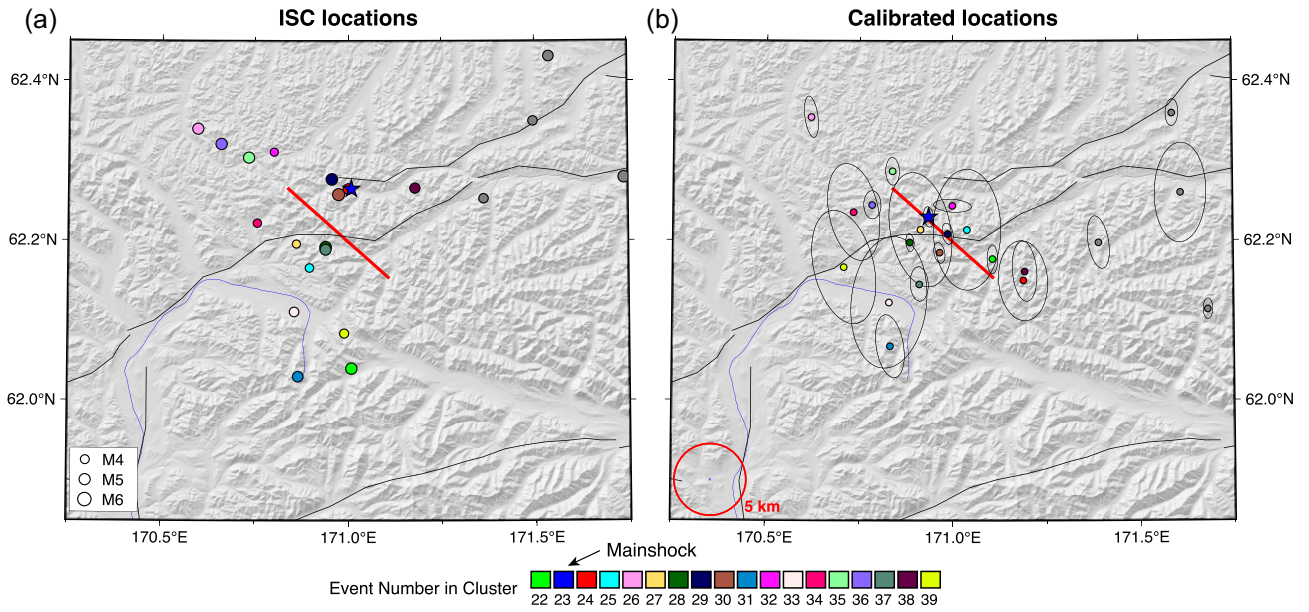


Figure 6. (a) Reported International Seismological Centre (ISC) epicentres and (b) relocated epicentres of the 2020 sequence, scaled by magnitude and numbered and coloured chronologically. These include one foreshock, the main shock (blue star), 11 aftershocks and a few other regional events (grey). The red line is our InSAR modelled fault and black lines are other regional faults (Zelenin *et al.* 2022). In (b), black ellipses are 90 per cent confidence ellipses for individual cluster vectors (i.e. relative locations) and red circle of radius 5 km is for scale.

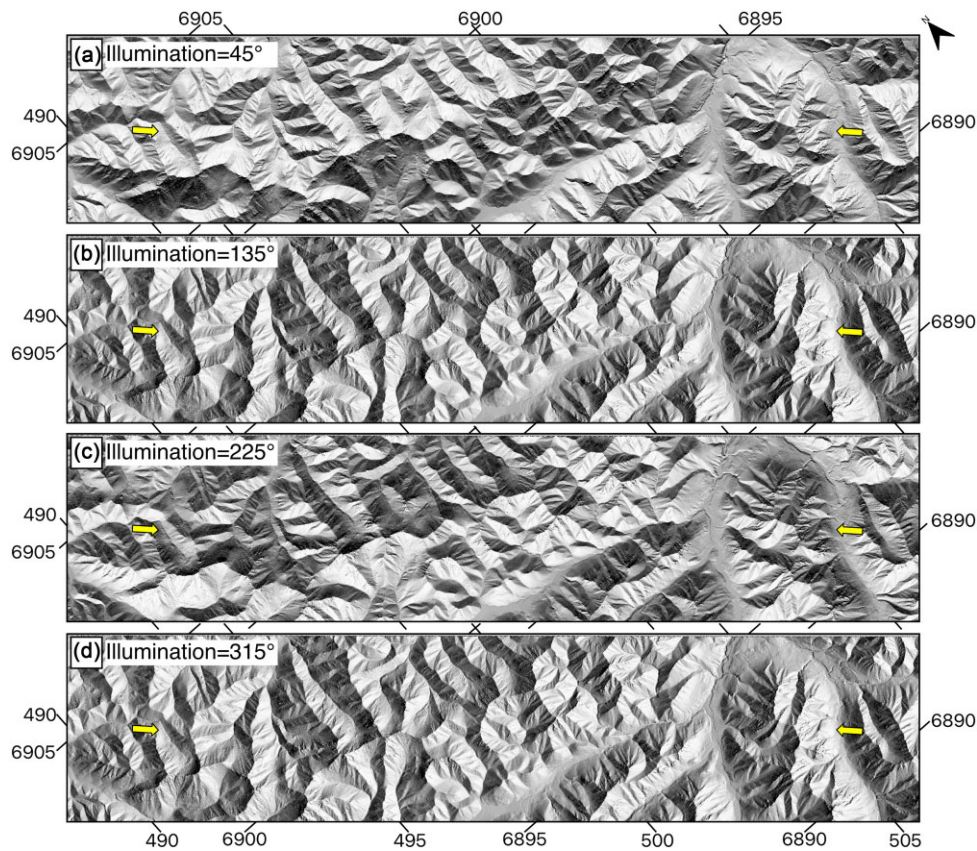


Figure 7. Hillshaded ArcticDEM topography (Porter *et al.* 2022) along our InSAR model fault (ends indicated by yellow arrows) with illumination from (a) 45°, (b) 135°, (c) 225° and (d) 315°. Coordinates are in UTM kilometres.

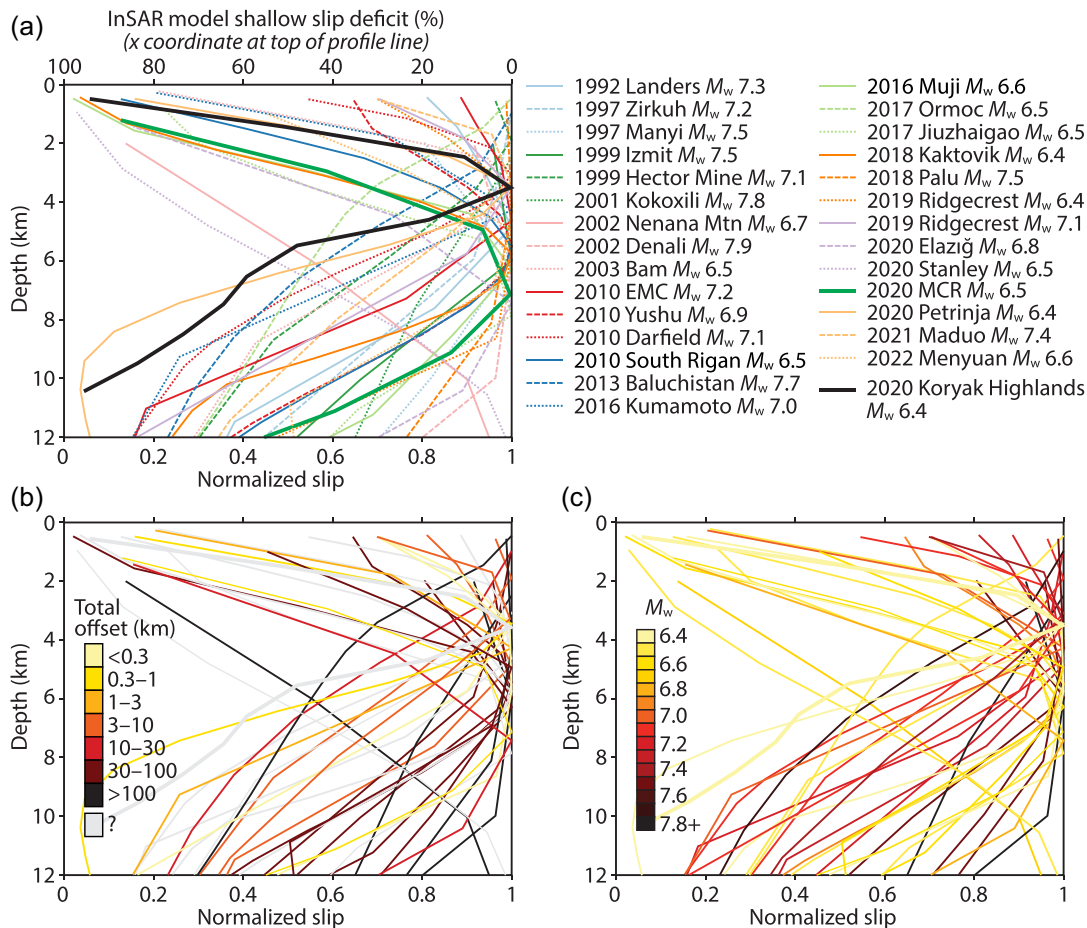


Figure 8. (a) Normalized slip profiles for the Koryak Highlands earthquake and 29 large (M_w 6.4–7.9) continental earthquakes with predominantly strike-slip motion and InSAR-derived coseismic slip models, modified from Sethanant *et al.* (2023). Model slip along each row of slip patches was averaged, normalized by dividing it by the maximum value of average slip, and plotted against depth. SSD values plotted along the top of the graph refer to the shallowest data points of the profile, and are equal to one minus the normalized slip of the surficial row of model subfault patches expressed as a percentage (e.g. Fialko *et al.* 2005). (b) Normalized slip profiles coloured by total geological offset along the host fault and (c) by earthquake moment magnitude; see Sethanant *et al.* (2023) for details of the other earthquakes.

pronounced SSDs are linked not by fault structural immaturity, but rather by their moderate magnitudes: strike-slip earthquakes only consistently rupture fully to the surface, no matter their nucleation depths, once they reach magnitudes greater than about 7.

4.2 Implications for active tectonics of the northern Pacific Cordillera

Due to the slow rates of deformation, sparse instrumentation and limited exposure to earthquakes, active tectonics and seismic hazards in the northern Pacific Cordillera are poorly understood relative to other major continental orogenic systems such as the main North American Cordillera or the Alpine-Himalayan belt. As one of the best-recorded earthquakes in the region up till now, the 2020 Koryak Highlands event therefore offers an important new point of reference.

One important parameter in continental tectonics is the seismogenic layer thickness, which varies from about 10 to 40 km across most orogenic belts (Maggi *et al.* 2000a). This parameter sets the lower depth limit for coseismic slip and thus helps control rupture area and magnitude. Routine earthquake catalogues are poor at resolving depths of crustal earthquakes and, outside of the most

densely instrumented regions, the best constraints on seismogenic layer thickness come from regional or teleseismic waveform modelling (Maggi *et al.* 2000b; Engdahl *et al.* 2006; Wimpenny & Watson 2021). Unfortunately, only a handful of large earthquakes across the northern Pacific Cordillera have centroid depths resolved in this manner, and even fewer have slip distributions constrained by geodetic data (Fig. 9), leaving the seismogenic thickness largely obscure.

Our InSAR analysis of the 2020 Koryak Highlands earthquake supports peak slip at 3–4 km depth, diminishing rapidly towards the base of the model fault plane at 11 km. Svigkas *et al.* (2023) yield a similar slip distribution but with small amounts of slip down to 14 km depth. Further SW within the Koryak Highlands, aftershocks of the 2006 M_w 7.6 Olyutorski earthquake recorded by three temporary local stations concentrate above about 18 km, but the main shock itself, and the largest aftershock (M_w 6.6), are poorly constrained (Lander *et al.* 2010).

Constraints on seismogenic layer thickness in the Koryak Highlands therefore remain sparse, but earthquake studies from Alaska and Canada suggest that, inboard of active forearcs, much of the northern Pacific Cordillera may be characterized by shallow (~10–15 km) seismicity. In northern Alaska, InSAR modelling of the

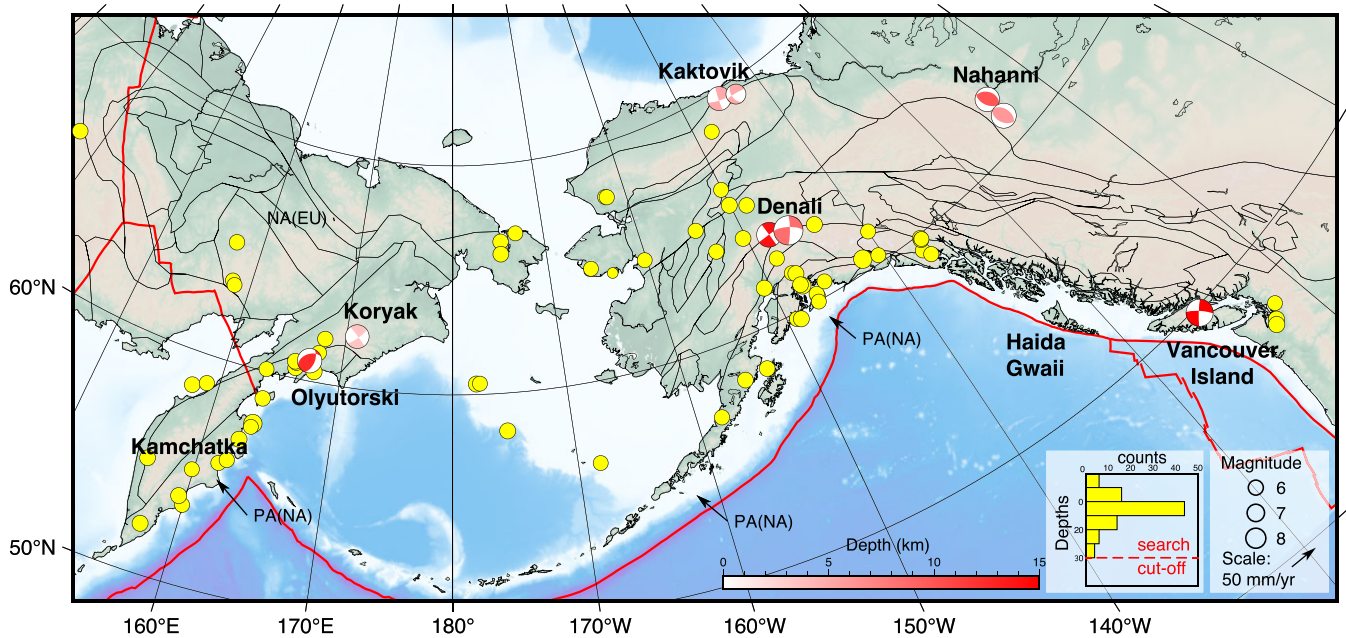


Figure 9. Terranes of the north Pacific Cordillera. Terrane boundaries, in black, are from a tectonic model of the Arctic (Shephard *et al.* 2013). Yellow circles indicate the location of large crustal earthquakes ($M > 6$, with depths < 30 km) within the north Pacific Cordillera. Many of these large events have occurred close to, or along, major structures. The histogram shows the depth distribution of these earthquakes. These events are from the ISC Bulletin for the period 1964–2024. Several notable events (discussed in the text) are labelled and coloured by the depth of maximum slip (Supporting Information, Table S3). Vectors show relative velocities of the Pacific (PA), North American (NA), Eurasia (EU) and Juan de Fuca (JF) plates from the ITRF2020 plate motion model (Altamimi *et al.* 2023).

2018 M_w 6.4 and 6.0 Kaktovik earthquakes reveals slip between about 2 and 9 km depth, and centroid moment tensors of aftershocks recorded by the US Array Transportable Array are similarly shallow (Gaudreau *et al.* 2019; Xu *et al.* 2020; Estève *et al.* 2022). In central Alaska, InSAR and global navigation satellite system (GNSS) models of the 2002 M_w 7.9 Denali earthquake exhibit peak slip within the upper ~ 10 km, diminishing rapidly to about 18 km depth (Wright *et al.* 2004; Hreinsdóttir *et al.* 2006; Elliott *et al.* 2007), consistent with locally recorded seismicity along the Denali fault (Eberhart-Phillips *et al.* 2003; Ratchkovski *et al.* 2004; Choi *et al.* 2021; Biegel *et al.* 2024). Older waveform-modelled earthquakes include the 1985 M_w 6.7 and 6.8 Nahanni doublet in the Mackenzie mountains of Canada, placed at 6–7 km centroid depth (Choy & Boatwright 1988), consistent with local aftershock surveys that indicate focal depths mostly above ~ 12 km (Horner *et al.* 1990). Additionally, the 1946 M_s 7.2 Vancouver Island earthquake was modelled by Rogers & Hasegawa (1978) to have a focal depth of 20–30 km. Subsequent geodetic (Slawson & Savage 1979) and palaeoseismic studies (Lynch *et al.* 2023) suggest that the peak slip of this event was shallow (< 5 km). The shallow seismicity across Alaska and northwestern Canada are likely the result of thinned backarc lithosphere and high heat flow (Hyndman 2023), and the limited results from the Koryak Highlands hint that the same may be true further west.

The regions that comprise the north Pacific Cordillera have undergone similar tectonic histories of terrane accretion, deformation, magmatism and batholith emplacement (Dickinson 2004; Miller *et al.* 2002), and many of the major crustal earthquakes listed above are closely associated with terrane boundaries along which crustal fragments accreted to North America during the Mesozoic and early Cenozoic (Fig. 9). For example, the 1991 M_w 6.7 and 2006 M_w 7.6 Olyutorski earthquakes ruptured the major Khatyrka–Vyvenka fault

zone, the 2002 Denali rupture closely follows the Mesozoic suture of the Wrangellia and Yukon terranes (Fitzgerald *et al.* 2014), and the 2018 Kaktovik earthquakes may have partially reactivated terrane-bounding reverse faults associated with construction or reactivation of the Brookes Range (Gaudreau *et al.* 2019). This suggests that these first-order geological boundaries form long-lasting zones of weakness along which seismic hazards remain elevated long after terrane accretion. However, in rupturing a fault in close proximity but orthogonal to a terrane boundary, the 2020 Koryak Highlands earthquake demonstrates that hazards are not restricted to the major terrane bounding faults, but encompass secondary faults with minimal geomorphic or geological signatures. Like many other parts of the northern Pacific Cordillera, the Koryak Highlands likely exhibits slow strain rates with faults that may have recurrence periods of thousands to tens of thousands of years (Li *et al.* 2018), such that Pleistocene glaciations may have eroded pre-existing geomorphic signals (e.g. Clague & James 2002). This is one of many challenges to studying slowly deforming faults in high latitude, sub-Arctic regions, along with sparse seismic and geodetic instrumentation, GNSS strain signals that are masked by locking of the subducting Pacific plate and/or by glacio-isostatic rebound, and remote, mountainous and densely forested terrain.

5 CONCLUSIONS

The 2020 M_w 6.4 Koryak Highlands earthquake ruptured a previously unknown, SE-striking, left-lateral strike-slip fault, orthogonal to the main sutures that bound the Khatyrka–Vyvenka zone. The earthquake likely propagated unilaterally northwestwards at approximately 1.3 km s^{-1} . This slow rupture speed, together with the lack of any clear fault-related geomorphology along the surface trace, indicates that the causative fault was structurally immature.

The earthquake also exhibits a pronounced SSD, though this may be related more to its moderate magnitude than to fault structural immaturity. The base of our slip model at 11 km depth hints at a relatively thin seismogenic layer thickness, consistent with other parts of the north Pacific Cordillera. Remote, mountainous and recently glaciated areas like the Koryak Highlands are particularly challenging to study, but modern, remotely sensed or teleseismic data still allow us to characterize the geometry and kinematics of this earthquake fairly precisely. Our study highlights how unknown or uncharacterized faults may accommodate potentially damaging earthquakes along or near terrane boundaries within the northern North America plate.

ACKNOWLEDGMENTS

This study is funded through grants from the Natural Sciences and Engineering Research Council of Canada (NSERC), the Canada Foundation for Innovation (CFI) and the BC Knowledge Development Fund (BCKDF), as well as a James A. and Laurette Agnew Memorial Award to Guy Salomon, and a Tier 2 Canada Research Chair to Edwin Nissen. The authors are grateful to Ezgi Karasözen, Lucinda Leonard and Andrew Schaeffer for discussions of this work, and Jeffrey Freymueller and an anonymous reviewer for comments that improved the manuscript.

SUPPORTING INFORMATION

Supplementary data are available at [GJIRAS](https://doi.org/10.1093/gji/ggaf031) online

distributed_slip_model.csv
Relocated_hypocenters.csv
Supplemental_Material.pdf

Please note: Oxford University Press is not responsible for the content or functionality of any supporting materials supplied by the authors. Any queries (other than missing material) should be directed to the corresponding author for the paper.

DATA AVAILABILITY

The supplemental material comprises of 11 figures (Figs S1–S11), 3 tables and 2 data files. The figures show satellite imagery for the region, additional results from the InSAR modelling, and additional plots from the *mloc* relocation. Tables include the fault parameters and their search bounds for the InSAR inverse and forward models and the normalized slip profile from the distributed slip model. Data files include the full distributed slip model and our relocated hypocenters. Descriptions of each data field (column) in the data files are included in the supplemental pdf document.

The images used to produce the interferograms are freely available and were downloaded from the ESA's open access hub (European Space Agency, 2020). Several topography data sets were used in this study, including the Copernicus GLO-30 DEM (European Space Agency, 2021), the GEBCO bathymetry data set (GEBCO Compilation Group, 2023) and 2 m resolution Arctic-DEM data along the InSAR fault (Porter et al. 2022), all of which are available on OpenTopography (<https://opentopography.org/>, last accessed 2024 July). Earthquake arrival times were collected from the International Seismological Centre (ISC) bulletin (<https://doi.org/10.31905/d808b825>). Focal mechanisms were downloaded from the Global Centroid-Moment-Tensor Project (Ekström et al. 2012). Figures were plotted using the Generic Mapping Tools, Version 6

(Wessel et al. 2019). Fault lines in figures were acquired from the Active Faults of Eurasia Database (AFEAD, Zelenin et al. 2022).

REFERENCES

- Akinin, V.V., Miller, E.L., Toro, J., Prokopiev, A.V., Gottlieb, E.S., Pearcey, S., Polzunenkov, G.O. & Trunilina, V.A., 2020. Episodicity and the dance of late Mesozoic magmatism and deformation along the northern circum-Pacific margin: north-eastern Russia to the Cordillera, *Earth-Sci. Rev.*, **208**, 103272, doi:10.1016/j.earscirev.2020.103272.
- Altamimi, Z., Métivier, L., Rebischung, P., Collilieux, X., Chanard, K. & Barnéoud, J., 2023. ITRF2020 plate motion model, *Geophys. Res. Lett.*, **50**(24), e2023GL106373, doi:10.1029/2023GL106373.
- Bergman, E.A. & Solomon, S.C., 1990. Earthquake swarms on the Mid-Atlantic Ridge: products of magmatism or extensional tectonics?, *J. geophys. Res.: Solid Earth*, **95**(B4), 4943–4965.
- Biegel, K.M., Gosselin, J.M., Dettmer, J., Colpron, M., Enkelmann, E. & Caine, J.S., 2024. Earthquake relocations delineate a discrete fault network and deformation corridor throughout southeast Alaska and southwest Yukon, *Tectonics*, **43**(5), e2023TC008140, doi:10.1029/2023TC008140.
- Bro, R. & De Jong, S., 1997. A fast non-negativity-constrained least squares algorithm, *J. Chemo. Soc.*, **11**(5), 393–401.
- Chekovich, V., Palandzhyan, S., Sukhov, A., Egorkin, A. & Ben'yamovsky, V., 2008. The Late Cretaceous-Paleogene active margin of Northeastern Asia: Geodynamic setting of terrigenous sedimentary basins in the Central Koryak terrane, *Geotectonics*, **42**(1), 48–63.
- Choi, M., Eaton, D.W. & Enkelmann, E., 2021. Is the Eastern Denali fault still active?, *Geology*, **49**(6), 662–666.
- Choy, G.L. & Boatwright, J., 1988. Teleseismic and near-field analysis of the Nahanni earthquakes in the Northwest Territories, Canada, *Bull. seism. Soc. Am.*, **78**(5), 1627–1652.
- Clague, J.J. & James, T.S., 2002. History and isostatic effects of the last ice sheet in southern British Columbia, *Quat. Sci. Rev.*, **21**(1–3), 71–87.
- Coney, P.J. & Evenchick, C.A., 1994. Consolidation of the American Cordilleras, *J. South Am. Earth Sci.*, **7**(3), 241–262.
- Dickinson, W.R., 2004. Evolution of the North American cordillera, *Annu. Rev. Earth planet. Sci.*, **32**, 13–45.
- Dolan, J.F. & Haravitch, B.D., 2014. How well do surface slip measurements track slip at depth in large strike-slip earthquakes? The importance of fault structural maturity in controlling on-fault slip versus off-fault surface deformation, *Earth planet. Sci. Lett.*, **388**, 38–47.
- Dziewonski, A.M., Chou, T.-A. & Woodhouse, J.H., 1981. Determination of earthquake source parameters from waveform data for studies of global and regional seismicity, *J. geophys. Res.: Solid Earth*, **86**(B4), 2825–2852.
- Eberhart-Phillips, D. et al., 2003. The 2002 Denali Fault Earthquake, Alaska: a large magnitude, slip-partitioned event, *Science*, **300**(5622), 1113–1118.
- Ekström, G., Nettles, M. & Dziewoński, A., 2012. The global CMT project 2004–2010: centroid-moment tensors for 13,017 earthquakes, *Phys. Earth planet. Inter.*, **200**, 1–9.
- Elliott, J., Nissen, E., England, P., Jackson, J.A., Lamb, S., Li, Z., Oehlers, M. & Parsons, B., 2012. Slip in the 2010–2011 Canterbury earthquakes, New Zealand, *J. geophys. Res.: Solid Earth*, **117**(B3), doi:10.1029/2011JB008868
- Elliott, J.L., Freymueller, J.T. & Rabus, B., 2007. Coseismic deformation of the 2002 Denali fault earthquake: Contributions from synthetic aperture radar range offsets, *J. geophys. Res. (Solid Earth)*, **112**(B6), doi:10.1029/2006JB004428
- Engdahl, E.R., Jackson, J.A., Myers, S.C., Bergman, E.A. & Priestley, K., 2006. Relocation and assessment of seismicity in the Iran region, *Geophys. J. Int.*, **167**(2), 761–778.
- Estève, C., Liu, Y., Koulakov, I., Schaeffer, A.J. & Audet, P., 2022. Seismic evidence for a weakened thick crust at the Beaufort Sea Continental Margin, *Geophys. Res. Lett.*, **49**(16), doi:10.1029/2022GL100158
- European Space Agency, 2020. *Copernicus Data Space Ecosystem*, from <https://dataspace.copernicus.eu/> (Accessed 21 July 2022).

- European Space Agency, 2021. *Copernicus Global Digital Elevation Model*. Distributed by OpenTopography. <https://doi.org/10.5069/G9028PQB> (Accessed 22 May 2022).
- Fialko, Y., Sandwell, D., Simons, M. & Rosen, P., 2005. Three-dimensional deformation caused by the Bam, Iran, earthquake and the origin of shallow slip deficit, *Nature*, **435**(7040), 295–299.
- Fitzgerald, P.G., Roeske, S.M., Benowitz, J.A., Riccio, S.J., Perry, S.E. & Armstrong, P.A., 2014. Alternating asymmetric topography of the Alaska range along the strike-slip Denali fault: strain partitioning and lithospheric control across a terrane suture zone, *Tectonics*, **33**(8), 1519–1533.
- Funning, G.J., Parsons, B., Wright, T.J., Jackson, J.A. & Fielding, E.J., 2005. Surface displacements and source parameters of the 2003 Bam (Iran) earthquake from Envisat advanced synthetic aperture radar imagery, *J. geophys. Res.: Solid Earth*, **110**(B9). doi:10.1029/2004jb003338
- Gaudreau, E., Nissen, E., Bergman, E.A., Benz, H.M., Tan, F. & Karasözen, E., 2019. The August 2018 Kaktovik earthquakes: active tectonics in northeastern Alaska revealed with InSAR and seismology, *Geophys. Res. Lett.*, **46**(24), 14412–14420.
- GEBCO Compilation Group, 2023. *GEBCO 2023 Grid*, from: <https://doi.org/10.5069/G9D21VTT> (Accessed 4 July 2024).
- Ghods, A., Rezapour, M., Bergman, E., Mortezanejad, G. & Talebian, M., 2012. Relocation of the 2006 M_w 6.1 Silakhour, Iran, earthquake sequence: details of fault segmentation on the main recent fault, *Bull. seism. Soc. Am.*, **102**(1), 398–416.
- Glushkova, O., 2011. Late Pleistocene Glaciations in North-East Asia, in *Quaternary Glaciations - Extent and Chronology*, Vol. **15**, pp. 865–875. eds Ehlers, Jürgen, Gibbard, Philip L. & Hughes, Philip D., Elsevier.
- Guo, H., Lay, T. & Brodsky, E.E., 2023. Seismological indicators of geologically inferred fault maturity, *J. geophys. Res.: Solid Earth*, **128**(10). doi:10.1029/2023JB027096
- Horner, R.B., Wetmiller, R.J., Lamontagne, M. & Plouffe, M., 1990. A fault model for the nahanni earthquakes from aftershock studies, *Bull. seism. Soc. Am.*, **80**(6A), 1553–1570.
- Heinsdóttir, S., Freymueller, J.T., Bürgmann, R. & Mitchell, J., 2006. Coseismic deformation of the 2002 Denali Fault earthquake: insights from GPS measurements, *J. geophys. Res. (Solid Earth)*, **111**(B3), doi:10.1029/2005JB003676
- Hyndman, R.D., 2023. The thermal regime of NW Canada and Alaska, and tectonic and seismicity consequences, *Geochem. Geophys. Geosyst.*, **24**(7), doi:10.1029/2022GC010570
- Imaeva, L.P., Gusev, G.S., Imaev, V.S., Ashurkov, S.V., Melnikova, V.I. & Seredkina, A.I., 2017. Geodynamic activity of modern structures and tectonic stress fields in northeast asia, *Geodyn. Tectonophys.*, **8**(4), 737–768.
- International Seismological Centre, 2024. *On-line Bulletin*, Thatcham, UK. <https://doi.org/10.31905/D808B830> (Accessed 8 October 2024).
- Jönsson, S., Zebker, H., Segall, P. & Amelung, F., 2002. Fault slip distribution of the 1999 M_w 7.1 Hector Mine, California, earthquake, estimated from satellite radar and GPS measurements, *Bull. seism. Soc. Am.*, **92**(4), 1377–1389.
- Jordan, T.H. & Sverdrup, K.A., 1981. Teleseismic location techniques and their application to earthquake clusters in the south-central Pacific, *Bull. seism. Soc. Am.*, **71**(4), 1105–1130.
- Kanamori, H. & Anderson, D.L., 1975. Theoretical basis of some empirical relations in seismology, *Bull. seism. Soc. Am.*, **65**, 1073–1095.
- Karasözen, E., Nissen, E., Bergman, E.A., Johnson, K.L. & Walters, R.J., 2016. Normal faulting in the Simav graben of western Turkey reassessed with calibrated earthquake relocations, *J. geophys. Res. (Solid Earth)*, **121**(6), 4553–4574.
- Kennett, B. & Engdahl, E., 1991. Traveltimes for global earthquake location and phase identification, *Geophys. J. Int.*, **105**(2), 429–465.
- Kiser, E. & Ishii, M., 2017. Back-projection imaging of earthquakes, *Annu. Rev. Earth planet. Sci.*, **45**(2017), 271–299.
- Lander, A.V., Bukchin, B.G., Kiryushin, A.V. & Droznin, D.V., 1996. The tectonic environment and source parameters of the Khailino, Koryakia Earthquake of March 8, 1991, in *Selected Papers from Volumes 26 and 27 of Vychislitel'naya Seysmologiya, Computational Seismology and Geodynamics*, pp. 80–96, Wiley Online Library.
- Lander, A.V., Levina, V.I. & Ivanova, E.I., 2010. The earthquake history of the Koryak Upland and the aftershock process of the M_w 7.6 April 20(21), 2006 Olyutorskii earthquake, *J. Volc. Seismol.*, **4**(2), 87–100.
- Li, G., Liu, Y., Regalla, C. & Morell, K.D., 2018. Seismicity relocation and fault structure near the Leech River fault zone, southern Vancouver Island, *J. geophys. Res.: Solid Earth*, **123**(4), 2841–2855.
- Lynch, E.M., Regalla, C.A., Morell, K.D., Harrichhausen, N. & Leonard, L.J., 2023. Late Pleistocene to Holocene transtension in the northern Cascadia forearc: evidence from surface ruptures along the Beaufort Range fault, *ESS Open Archive* doi:10.22541/essoar.168614686.67638260/v1
- Maggi, A., Jackson, J.A., McKenzie, D. & Priestley, K., 2000a. Earthquake focal depths, effective elastic thickness, and the strength of the continental lithosphere, *Geology*, **28**(6), 495, doi:10.1130/0091-7613(2000)28<495:EFDEET>2.0.CO;2
- Maggi, A., Jackson, J.A., Priestley, K. & Baker, C., 2000b. A re-assessment of focal depth distributions in southern Iran, the Tien Shan and northern India: do earthquakes really occur in the continental mantle?, *Geophys. J. Int.*, **143**(3), 629–661.
- McCaffrey, R. & Abers, G., 1988. *SYN3: A Program for Inversion of Teleseismic Body Waveform on Microcomputers, Air Force Geophysics Laboratory Technical Report*, Tech. Rep., AFGL-TR-88-0099, doi:10.21236/ADA198940.
- McCaffrey, R., Abers, G., Zwick, P. & Lee, W., 1991. Inversion of teleseismic body waves, *IASPEI Softw. Lib.*, **3**, 81–166.
- Meng, L., Ampuero, J.-P., Luo, Y., Wu, W. & Ni, S., 2012. Mitigating artifacts in back-projection source imaging with implications for frequency-dependent properties of the Tohoku-Oki earthquake, *Earth Planets Space*, **64**(12), 1101–1109.
- Mikhailov, V.O., Timoshkina, E.P., Diament, M. & Smirnov, V.B., 2023. Enigma of the Olyutorskii Earthquake resolved by SAR interferometry, *Pure appl. Geophys.*, **180**(10), 3423–3433.
- Miller, E.L., Gelman, M., Parfenov, L. & Hourigan, J., 2002. Tectonic setting of Mesozoic magmatism: A comparison between northeastern Russia and the North American Cordillera, in *Tectonic Evolution of the Bering Shelf-Chukchi Sea-Artic Margin and Adjacent Landmasses*, Vol. **360**, eds Miller, E.L., Grantz, A. & Klempner, S.L., Geological Society of America.
- Molnar, P. & Lyon-Caen, H., 1989. Fault plane solutions of earthquakes and active tectonics of the Tibetan Plateau and its margins, *Geophys. J. Int.*, **99**(1), 123–153.
- Nissen, E., Jackson, J., Jahani, S. & Tatar, M., 2014. Zagros “phantom earthquakes” reassessed—the interplay of seismicity and deep salt flow in the Simply Folded Belt?, *J. geophys. Res. (Solid Earth)*, **119**(4), 3561–3583.
- Okada, Y., 1985. Surface deformation due to shear and tensile faults in a half-space, *Bull. seism. Soc. Am.*, **75**(4), 1135–1154.
- Perrin, C., Manighetti, I., Ampuero, J.-P., Cappa, F. & Gaudemer, Y., 2016. Location of largest earthquake slip and fast rupture controlled by along-strike change in fault structural maturity due to fault growth, *J. geophys. Res.: Solid Earth*, **121**(5), 3666–3685.
- Perrin, C., Waldhauser, F. & Scholz, C.H., 2021. The shear deformation zone and the smoothing of faults with displacement, *J. geophys. Res. (Solid Earth)*, **126**(5), doi:10.1029/2020JB020447
- Porter, C. et al., 2022. *ArcticDEM - Strips, Version 4.1*, Harvard Dataverse, <https://doi.org/10.7910/DVN/C98DVS> Accessed 2 July 2024.
- Press, W.H., William, H., Teukolsky, S.A., Saul, A., Vetterling, W.T. & Flannery, B.P., 2007. *Numerical Recipes 3rd edition: The Art of Scientific Computing*, Cambridge University Press.
- Ratchkovski, N.A., S.W. & A.H.R., 2004. Seismotectonics of the Central Denali Fault, Alaska, and the 2002 Denali Fault earthquake sequence, *Bull. seism. Soc. Am.*, **94**(6B), S156–S174.
- Rogers, G.C. & Hasegawa, H.S., 1978. A second look at the British Columbia earthquake of June 23, 1946, *Bull. seism. Soc. Am.*, **68**(3), 653–676.
- Rogozhin, E.A., Gordeev, E.I. & Chebrov, V.N., 2007. The Koryak strong earthquake of April 20 (21), 2006: preliminary results, *Izv. Phys. Solid Earth*, **43**(2), 103–110.

- Rogozhin, E.A., Ovsyuchenko, A.N., Lutikov, A.I., Ruzaykin, A.I., Dontsova, G.Y. & Sysolin, A.I., 2021. The Koryak Earthquake: an example of a successfully predicted seismic event, *Seism. Instrum.*, **57**(1), 88–96.
- Schimmel, M. & Paulssen, H., 1997. Noise reduction and detection of weak, coherent signals through phase-weighted stacks, *Geophys. J. Int.*, **130**(2), 497–505.
- Sethanant, I., Nissen, E., Pousse-Beltran, L., Bergman, E. & Pierce, I., 2023. The 2020 Mw 6.5 Monte Cristo Range, Nevada, Earthquake: anatomy of a crossing-fault rupture through a region of highly distributed deformation, *Bull. seism. Soc. Am.*, **113**(3), 948–975.
- Shephard, G.E., MÅller, R.D. & Seton, M., 2013. The tectonic evolution of the Arctic since Pangea breakup: integrating constraints from surface geology and geophysics with mantle structure, *Earth-Sci. Rev.*, **124**, 148–183.
- Simons, M., Fialko, Y. & Rivera, L., 2002. Coseismic deformation from the 1999 M w 7.1 Hector Mine, California, earthquake as inferred from InSAR and GPS observations, *Bull. seism. Soc. Am.*, **92**(4), 1390–1402.
- Slawson, W.F. & Savage, J.C., 1979. Geodetic deformation associated with the 1946 Vancouver Island, Canada, earthquake, *Bull. seism. Soc. Am.*, **69**(5), 1487–1496.
- Svigkas, N., Atzori, S., Kozhurin, A., Tolomei, C., Antonioli, A. & Pezzo, G., 2023. Implications for the geometry of plate boundaries in NE Asia based on the geodetic analysis of the 2020 Mw 6.4 Koryak event, *Geophys. J. Int.*, **234**(2), 1412–1421.
- Tan, F., Ge, Z., Kao, H. & Nissen, E., 2019. Validation of the 3-D phase-weighted relative back projection technique and its application to the 2016 Mw 7.8 Kaikōura earthquake, *Geophys. J. Int.*, **217**(1), 375–388.
- Walker, R., Bergman, E., Szeliga, W. & Fielding, E., 2011. Insights into the 1968–1997 Dasht-e-Bayaz and Zirkuh earthquake sequences, eastern Iran, from calibrated relocations, InSAR and high-resolution satellite imagery, *Geophys. J. Int.*, **187**(3), 1577–1603.
- Wang, L., Marzahn, P., Bernier, M. & Ludwig, R., 2020. Sentinel-1 InSAR measurements of deformation over discontinuous permafrost terrain, Northern Quebec, Canada, *Remote Sens. Environ.*, **248**, 111965, doi:10.1016/j.rse.2020.111965.
- Wei, S., Barbot, S., Graves, R., Lienkaemper, J.J., Wang, T., Hudnut, K., Fu, Y. & Helmberger, D., 2015. The 2014 Mw 6.1 South Napa Earthquake: a unilateral rupture with shallow asperity and rapid afterslip, *Seismol. Res. Lett.*, **86**(2A), 344–354.
- Werner, C., Wegmüller, U., Strozzi, T. & Wiesmann, A., 2000. Gamma SAR and interferometric processing software, in *Proceedings of the ERS-Envisat Symposium, Gothenburg, Sweden*, Vol. **1620**, p. 1620, Citeseer.
- Werner, C., Wegmüller, U., Strozzi, T. & Wiesmann, A., 2002. Processing strategies for phase unwrapping for INSAR applications, in *Proceedings of the European Conference on Synthetic Aperture Radar EUSAR*.
- Wessel, P., Luis, J.F., Uieda, L., Scharroo, R., Wobbe, F., Smith, W.H.F. & Tian, D., 2019. The Generic Mapping Tools Version 6, *Geochem. Geophys. Geosyst.*, **20**(11), 5556–5564.
- Wetmiller, R.J., Horner, R.B., Hasegawa, H.S., North, R.G., Lamontagne, M., Weichert, D.H. & Evans, S.G., 1988. An analysis of the 1985 Nahanni earthquakes, *Bull. seism. Soc. Am.*, **78**(2), 590–616.
- Wimpenny, S. & Watson, C.S., 2021. gWFM: a global catalog of moderate-magnitude earthquakes studied using teleseismic body waves, *Seismol. Res. Lett.*, **92**(1), 212–226.
- Wright, T., Parsons, B., Jackson, J., Haynes, M., Fielding, E., England, P. & Clarke, P., 1999. Source parameters of the 1 October 1995 Dinar (Turkey) earthquake from SAR interferometry and seismic bodywave modelling, *Earth planet. Sci. Lett.*, **172**(1–2), 23–37.
- Wright, T.J., Lu, Z. & Wicks, C., 2004. Constraining the slip distribution and fault geometry of the M w 7.9, 3 November 2002, Denali fault earthquake with interferometric synthetic aperture radar and global positioning system data, *Bull. seism. Soc. Am.*, **94**(6B), S175–S189.
- Xu, G., Xu, C., Wen, Y., Xiong, W. & Valkaniotis, S., 2020. The Complexity of the 2018 Kaktovik Earthquake Sequence in the Northeast of the Brooks Range, Alaska, *Geophys. Res. Lett.*, **47**(19), doi:10.1029/2020GL088012
- Colpron, M. & Nelson, J.L., *A Digital Atlas of Terranes for the Northern Cordillera, Yukon Geological Survey*, 2011. www.geology.gov.yk.ca (Accessed 5 November 2023).
- Zaccagnino, D. & Doglioni, C., 2022. The impact of faulting complexity and type on earthquake rupture dynamics, *Commun. Earth Environ.*, **3**(1), 258, doi:10.1038/s43247-022-00593-5.
- Zelenin, E., Bachmanov, D., Garipova, S., Trifonov, V. & Kozhurin, A., 2022. The Active Faults of Eurasia Database (AFEAD): the ontology and design behind the continental-scale dataset, *Earth Syst. Sci. Data*, **14**(10), 4489–4503.
- Zhang, H. & Ge, Z., 2010. Tracking the rupture of the 2008 Wenchuan earthquake by using the relative back-projection method, *Bull. seism. Soc. Am.*, **100**(5B), 2551–2560.
- Zwack, P., McCaffrey, R. & Abers, G., 1994. MT5 program, *IASPEI Soft. Lib.*, **4**.